Weakened Hydrogen Bond Connectivity Promotes Interfacial Mass Transfer for Industrial Level Scalable Biomass Electrooxidation

Zhaohui Yang,[a] Lan Chen,[b,c] Yijun Yin,[a] Chenyang Wei,[a] Zhimin Xue,[b]

Tiancheng Mu*[a]

a Dr. Z. Yang, Dr. Y. Yin, Dr. C. Wei, and Prof. T. Mu

School of Chemistry and Life Resources, Renmin University of China, Beijing 100872, China. E-mail: tcmu@ruc.edu.cn

b Dr. L. Chen, Prof. Z. Xue

Beijing Key Laboratory of Lignocellulosic Chemistry, College of Materials Science and Technology, Beijing Forestry University, Beijing 100083, China. E-mail: zmxue@bjfu.edu.cn

c Dr. L. Chen

School of Chemistry and Chemical Engineering, Henan Normal University, Xinxiang, Henan 453007, China.

EXPERIMENTAL SECTION

Materials: Ammonium persulfate (98+%, Macklin), Nickel chloride (99%, Macklin), Sodium thiosulfate (99%, Aladdin), Sodium hydroxide (98%, Alfa) 5-Hydroxymethylfurfural (99%, Aladdin; 99+%, obtained from Zhongke Guosheng (Hangzhou) Technology Co., Ltd; 95%, Macklin), 2,5-furandicarboxaldehyde (98%, Innochem), 5-formylfuran-2-carboxylic acid (98%, Innochem), 5-hydroxymethyl- 2-furancarboxylic acid (98%, Innochem), 2,5-Furandicarboxylic acid (99%, Innochem), Methanol (99.9%, Innochem), ammonium formate (99%, Aladdin), ethanol (99.7%, SCR), acetone (99.5%, Acros), milli-Q water (18.2 MΩ), Copper foam (thickness 1.5 mm) purchased by Suzhou Keshenghe Metal Materials were used without further purification.

Preparation of electrode: A piece of copper foam (2 × 3 cm^2) was cleaned by acetone, 3 M HCl ethanol and DI water for 10 min, respectively. 0.2g $(NH_4)_2S_2O_8$, 0.45g NaOH, were mixed in 30 ml DI water, after stirring, Cu foam was immersed in it for 30 min, then taken out and washed by DI water to obtain $Cu(OH)_2$/CF. 0.48g $NiCl_2{\cdot}6H_2O$ and 0.6g $Na_2S_2O_3$ was mixed in 30 ml DI water, immersing $Cu(OH)_2$/CF in it and soak it at 80°C for 1h to obtain $Ni(OH)_2/Cu(OH)_2$/CF.

Electrochemical measurements: The electrochemical performance were tested by a CS350M workstation with standard three-electrode system consisted of as-prepared electrodes (1 × 1 cm^2) as working electrode, a carbon rod and Hg/HgO were used as counter and reference electrode, respectively. All tests were performed in H-type cell with FAA-3-50 membrane as the separator. The linear sweep voltammetry (LSV) was conducted at the scan rate of 5 mV s^{-1} with 90% iR correction. The electrochemically active surface area (ECSA) was obtained from the electrical double layer specific capacitor (C_{dl}). Cyclic voltammetry (CV) measurements were conducted in a non-faradaic potential range at different scan rates from 20 to 100 mV s^{-1} to acquire C_{dl}. Electrochemical impedance spectroscopy (EIS) was measured from 0.01 to 10^5 Hz. *In-situ* Raman was performed on an Xplora Plus Raman instrument with a 10x objective. Raman frequencies were firstly calibrated by Si wafer (520.6 cm^{-1}). A laser power was 1.5 mW and the lines were 638 nm. It took 30 s to obtain one spectrum each time with two accumulations. The electrochemical signal was input through CS350M, and Ag/AgCl and Pt wire were used as reference electrodes and

counter electrodes respectively in the Raman cell.

XAFS Experiment and Data Processing: XAFS measurements at Ni/Cu k-edge in both transmission and fluorescence (for samples) mode were performed at Hard X-ray branch of the E-line (BL20U1) in Shanghai Synchrotron Radiation Facility (SSRF). The electron beam energy was 3.5 GeV and the stored current was 200 mA (top-up). The hard X-ray branch of energy material beamline (E-line) with a photon flux of 2×1012 photons/s (0.1%BW) at 5 keV and a beam size of 80×20 μm is generated from 24-pole in-vacuum undulators. XAFS data were collected using a fixed-exit double-crystal Si(111) monochromator. A Lytle detector was used to collect the fluorescence signal, and the energy was calibrated using Ni/Cu foil. The raw data analysis was performed using IFEFFIT software package according to the standard data analysis procedures. The spectra were calibrated, averaged, pre-edge background subtracted, and post-edge normalized using Athena program in IFEFFIT software package. The Fourier transformation of the k^3-weighted EXAFS oscillations, $k^3 \cdot \chi(k)$, from k space to R space was performed to obtain a radial distribution function. And data fitting was done by Artemis program in IFEFFIT.

HPLC analysis of products: HMF and its oxidation products (HMFCA, FFCA, DFF, FDCA) were analyzed by high-performance liquid chromatography (HPLC, LC3000I system with an ultraviolet-visible detector and a 4.6 mm × 250 mm AQ-C18 column). In a typical measurement, a 10 μL aliquot of electrolyte was collected during electrolytic process, diluted to 3 mL with methanol and 5 mM ammonium formate solution (3:7), and then injected into HPLC column for analysis. As for the detecting conditions, the HPLC column temperature was maintained at 35 ◦C, while the flow rate is 0.6 ml/min, and the wavelength of UV detection is 265 nm. The HMF conversion, FDCA selectivity and faradaic efficiency were calculated according to the following equations:

$$\text{HMF conversion (\%)} = n\text{ (consumed HMF)} / n\text{ (initial HMF)} \times 100\%$$

$$\text{FDCA selectivity (\%)} = n\text{ (FDCA formed)} / n\text{ (consumed HMF)} \times 100\%$$

$$\text{Faradic efficiency (\%)} = 6 \times n\text{ (FDCA formed)} \times F / \text{total charge passed} \times 100\%$$

DFT calculations: The spin-polarized density functional theory (DFT) calculations were carried out in the Vienna ab initio simulation package (VASP) based on the plane-wave basis sets with the

projector augmented-wave method. The exchange-correlation potential was treated by using a generalized gradient approximation (GGA) with the Perdew-Burke-Ernzerhof (PBE) parametrization. The energy cutoff was set to be 450 eV. The Brillouin-zone integration was sampled with a Γ-centered Monkhorst-Pack mesh of 2 × 2 × 1 by VASPKIT. The structures were fully relaxed until the maximum force on each atom was less than 0.05 eV/Å, and the energy convergent standard was 10^{-5} eV. The van der Waals correction of Grimme's DFT-D3 model was also adopted. To avoid the periodic interactions for interface structures, a vacuum layer as large as 15 Å is used along the c direction normal to the interface.

Molecular dynamics simulation: The initial structure was built using the amorphous cell module of materials studio software, in which 3000 H_2O molecules, 3 HMF molecules, 48 KOH molecules, $Cu(OH)_2$ and $Ni(OH)_2$ were subjected to 2×2×1 supercells. The initial structure geometry was optimized using the Forcite module of materials studio, the calculation was set with an energy convergence condition of 1.0×10^{-4}, a maximum number of iteration steps of 500, Universal force field, atomic charges calculated by the Qeq method, atom-based Ewald method describing the electrostatic potential and van der Waals forces, and the truncation radius was set to 9Å. Dynamics simulations were performed using the Forcite module of materials studio, 15000 ps dynamics simulations at 298.0k, 1.0×10^{-4}Gpa, outputting geometrical configurations every 5000 steps, using the NVT synthesis, calculated using Universal Forcefield. Intermolecular interactions, atom based Ewald method to describe electrostatic potential and van der Waals forces, truncation radius set to 7.5Å, voltage 1.45 V added by script.

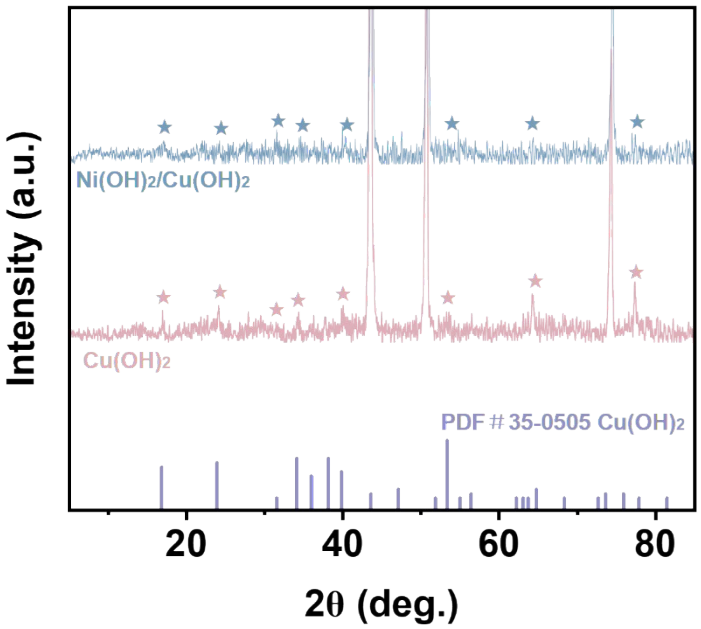

Fig. S1. XRD patterns of $Cu(OH)_2$/CF and $Ni(OH)_2/Cu(OH)_2$/CF.

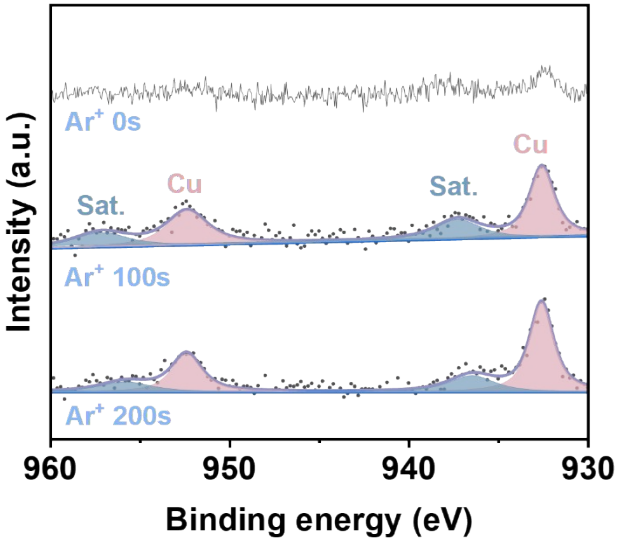

Fig. S2. High-resolution XPS spectra of Cu 2p for Ni(OH)2/Cu(OH)2 with different etching times by Ar^+.

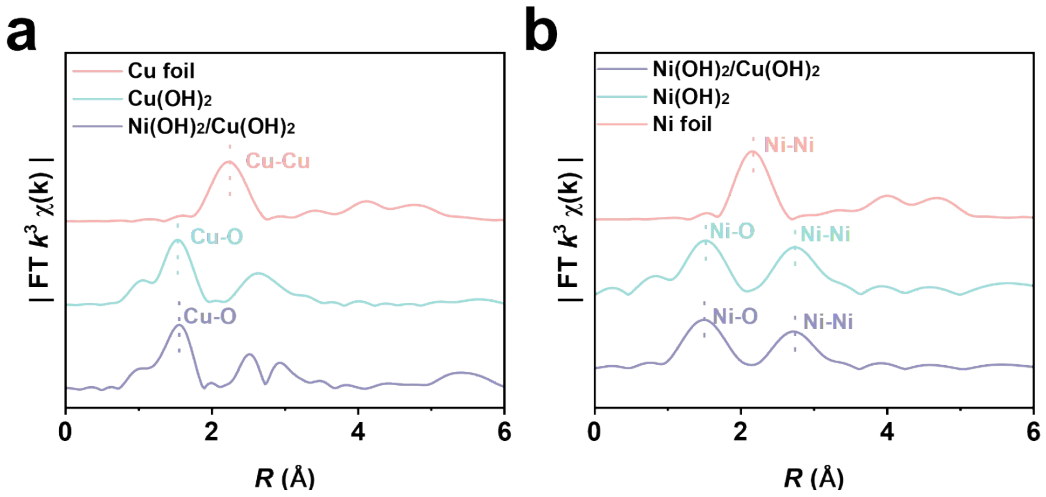

Fig. S3. Fourier transformation curves of EXAFS spectra at the (a) Cu K-edge and (b) Ni K-edge in the R-space for $Ni(OH)_2/Cu(OH)_2$ and $Cu(OH)_2$.

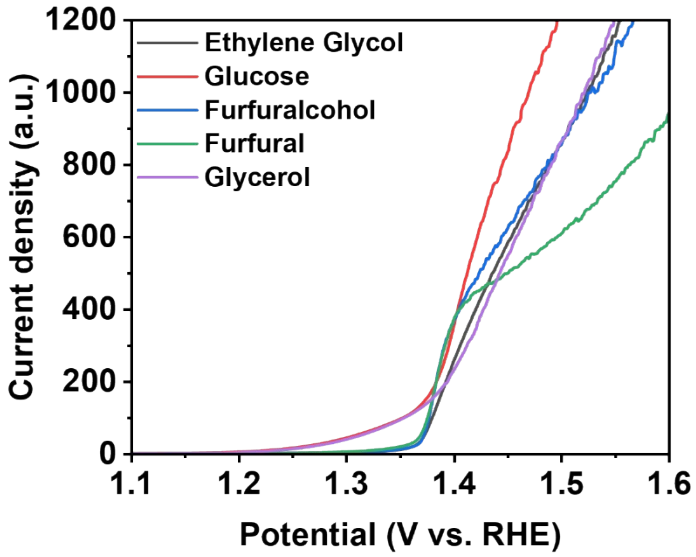

Fig. S4. LSV curves of Ni(OH)2/Cu(OH)2 in 1 M KOH with 50 mM Ethylene Glycol, Glucose, Furfuralcohol, Furfural and Glycerol, respectively.

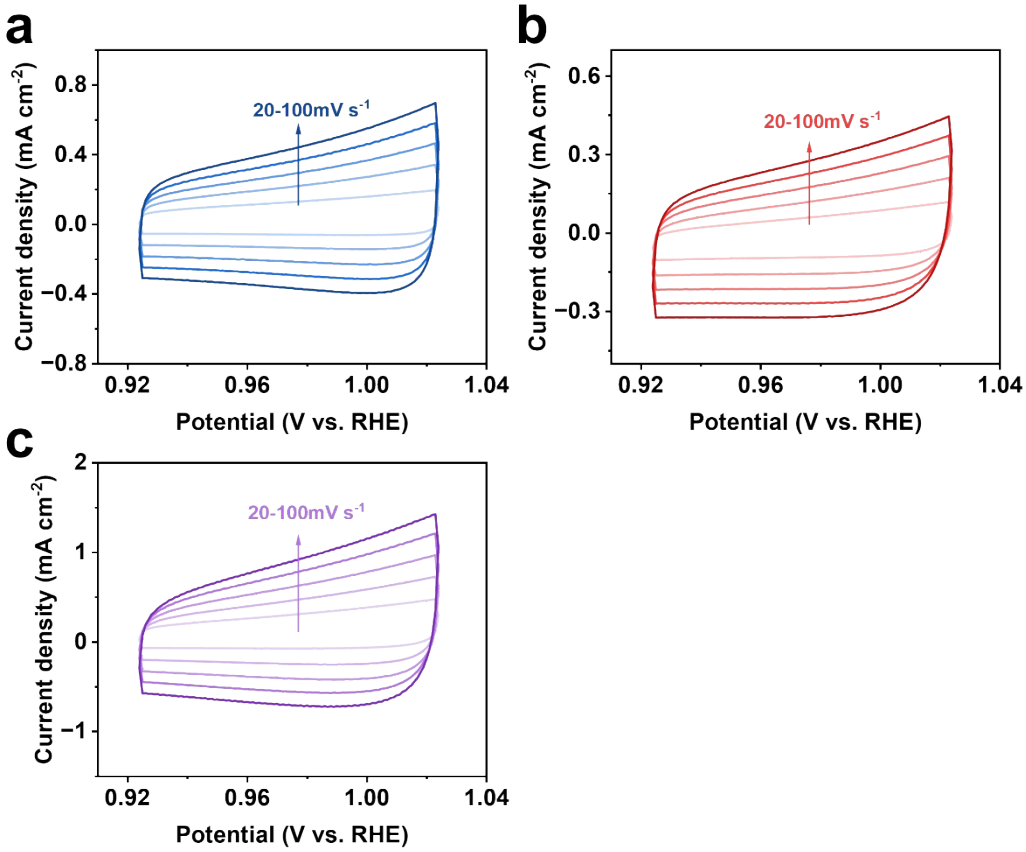

Fig. S5. CV curves of (a) $Cu(OH)_2$, (b) $Ni(OH)_2$ and (c) $Ni(OH)_2/Cu(OH)_2$ at different scan rates in non-Faradic interval.

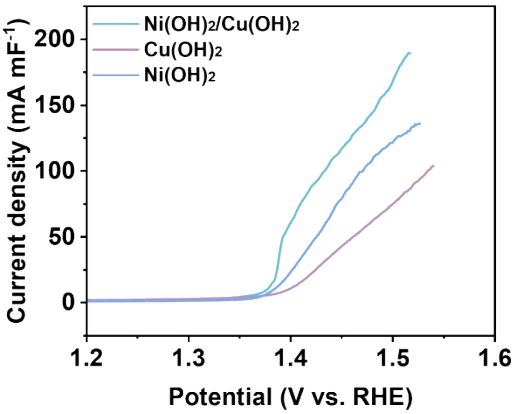

Fig. S6. LSV curves for HMFOR normalized by ECSA.

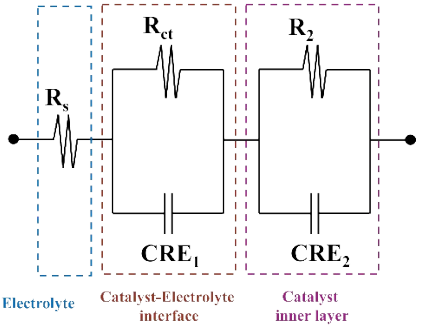

Fig. S7. The equivalent circuit image. R_s stands for the electrolyte resistance, CPE_1 represents double layer capacitance, R_{ct} has contact with the interfacial charge transfer reaction, CPE_2 and R_2 are related to the dielectric properties and the resistance of the electrode itself.

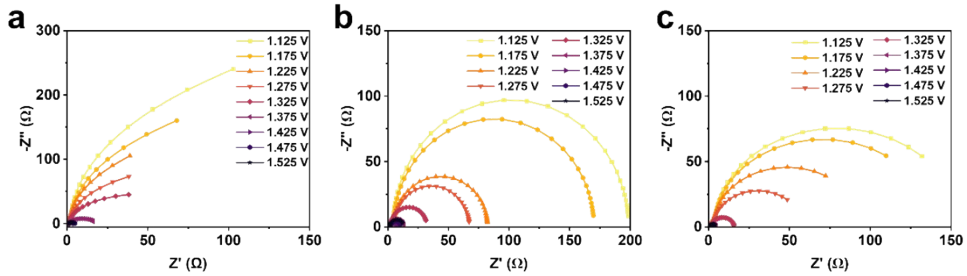

Fig. S8. The electrochemical impedance spectroscopy of (a) $Cu(OH)_2$, (b) $Ni(OH)_2$ and (c) $Ni(OH)_2$/ $Cu(OH)_2$ at different potentials.

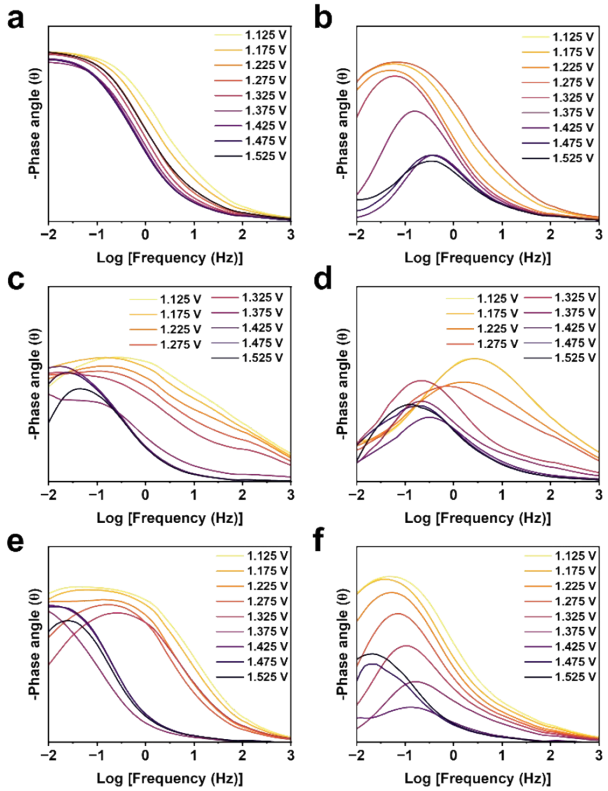

Fig. S9. Bode plots of the in-situ electrochemical impedance spectra of (a-b) $Cu(OH)_2$, (c-d) $Ni(OH)_2$ and (e-f) $Ni(OH)_2$/ $Cu(OH)_2$ in 1 M KOH with (a, c, e) or without (b, d, f) 50 mM HMF.

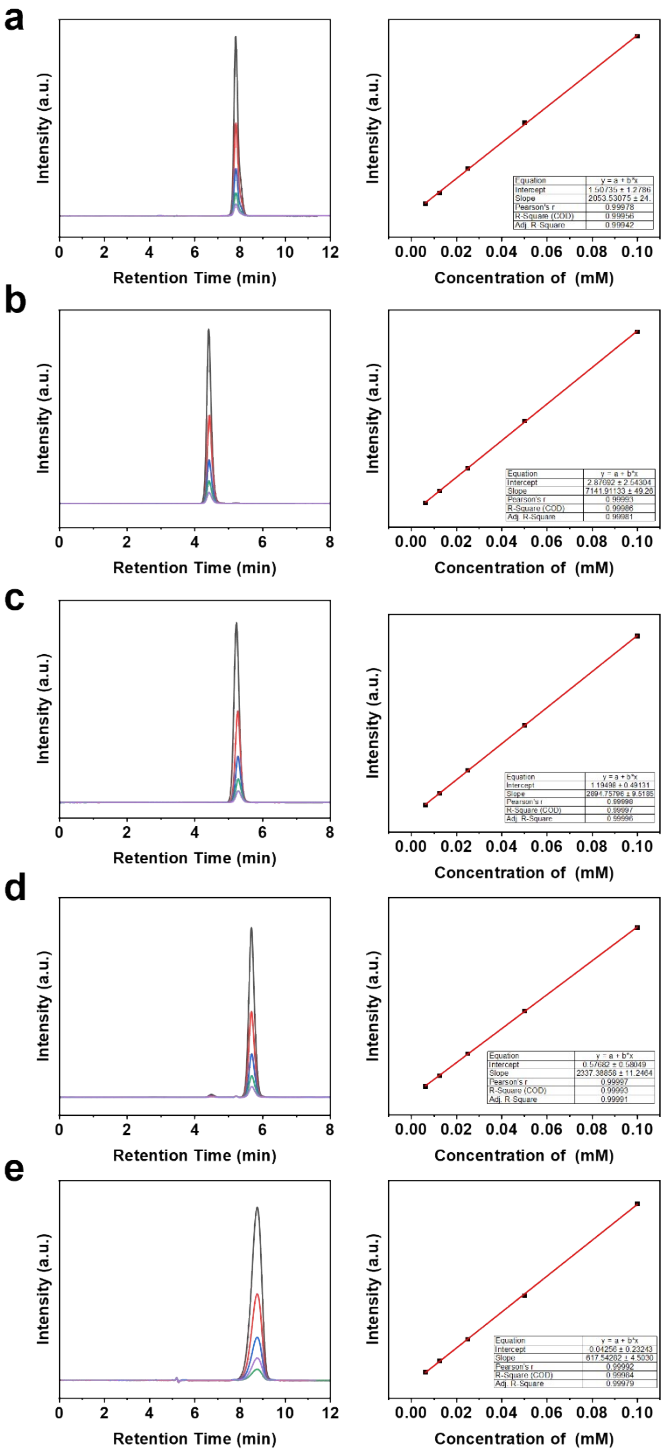

Fig. S10. Calibration of the HPLC for (a) HMF, (b) FDCA, (c) HMFCA, (d) FFCA and (e) DFF.

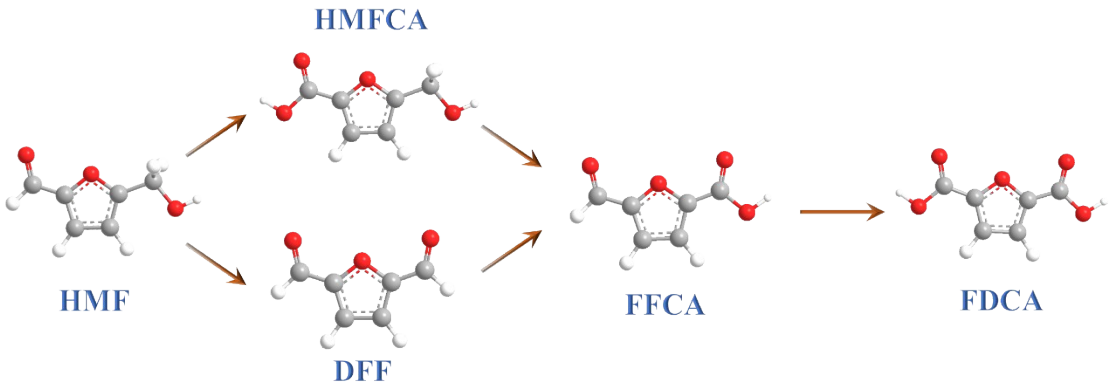

Fig. S11. Two possible routes of HMF oxidized to FDCA.

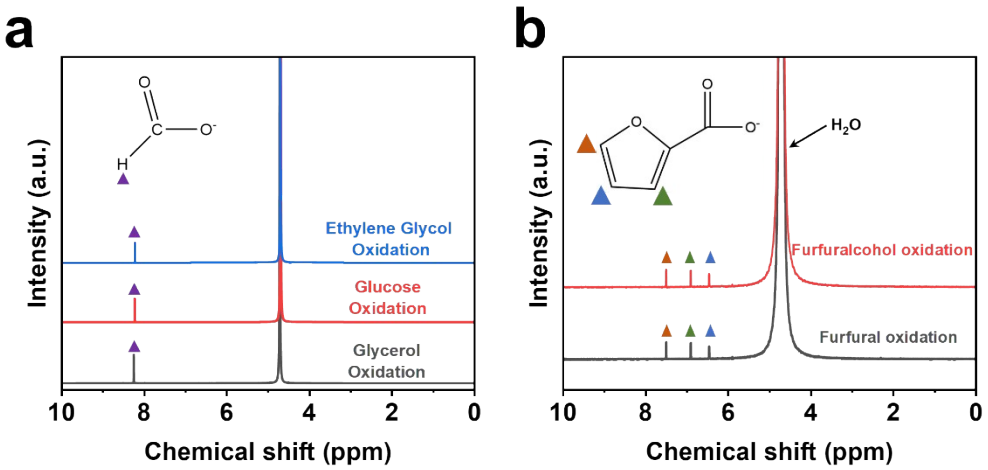

Fig. S12. (a) ^{1}H NMR spectra of formic acid obtained from Ethylene glycol, Glucose and Glycerol; (b) ^{1}H NMR spectra of furoic acid obtained from Furfuralcohol and Furfural.

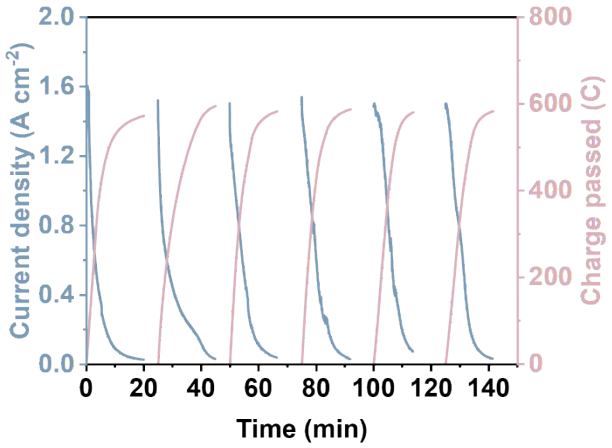

Fig. S13. Current density and charge-time plots for six cycles of electrolysis experiment on $Ni(OH)_2/Cu(OH)_2$.

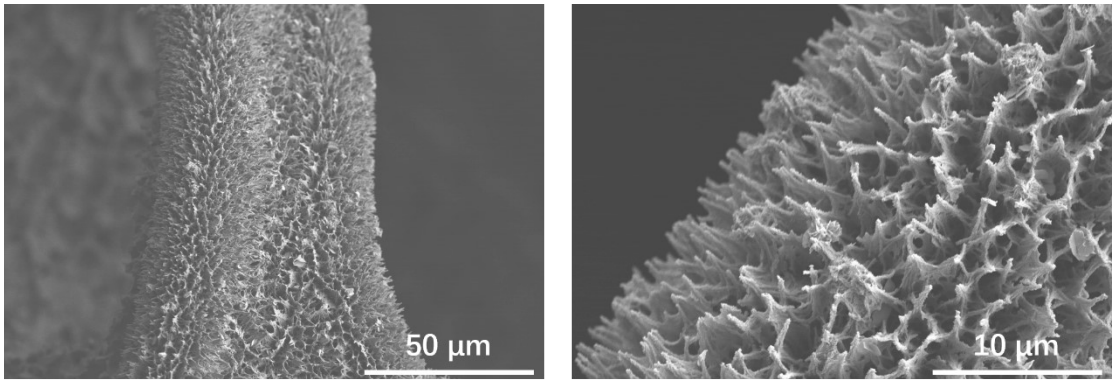

Fig. S14. SEM images of $Ni(OH)_2/Cu(OH)_2$ after stability test.

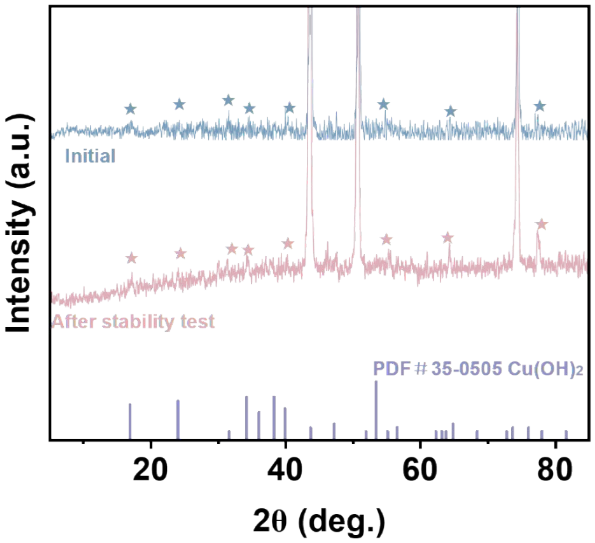

Fig. S15. XRD patterns of $Ni(OH)_2/Cu(OH)_2$ before and after stability test.

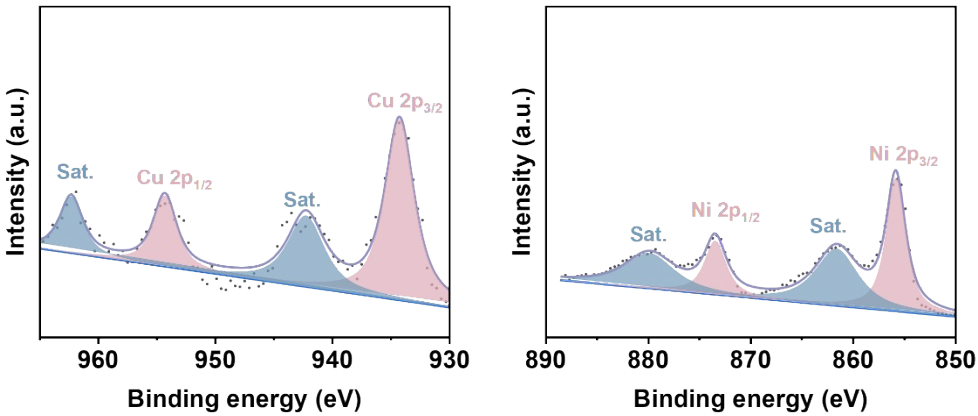

Fig. S16. High-resolution XPS spectra of Cu 2p and Ni 2p for $Ni(OH)_2/Cu(OH)_2$ after stability test.

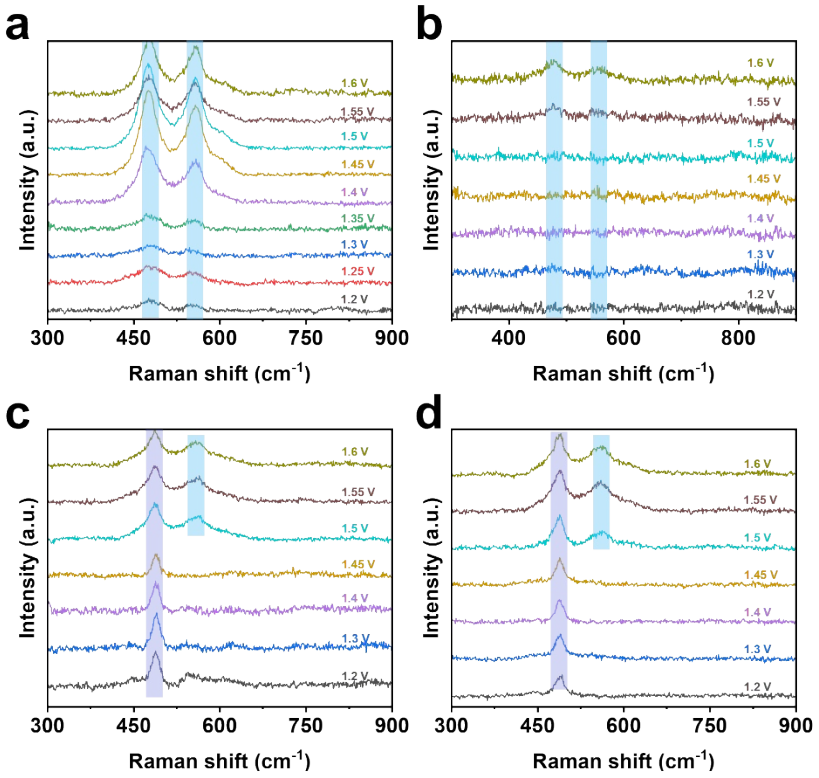

Fig. S17. In-situ Raman spectra of (a-b) $Ni(OH)_2$ and (c-d) $Cu(OH)_2$ at different potentials in OER (a, c) and HMFOR (b, d) system

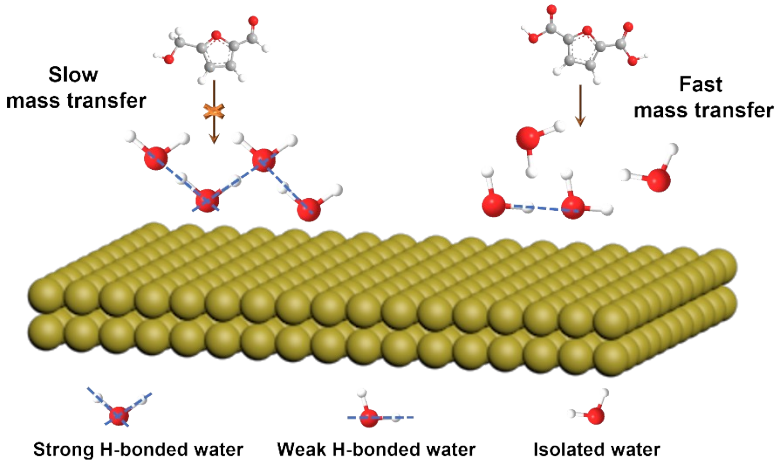

Fig. S18. Schematics of hydrogen bonding structure of interfacial water.

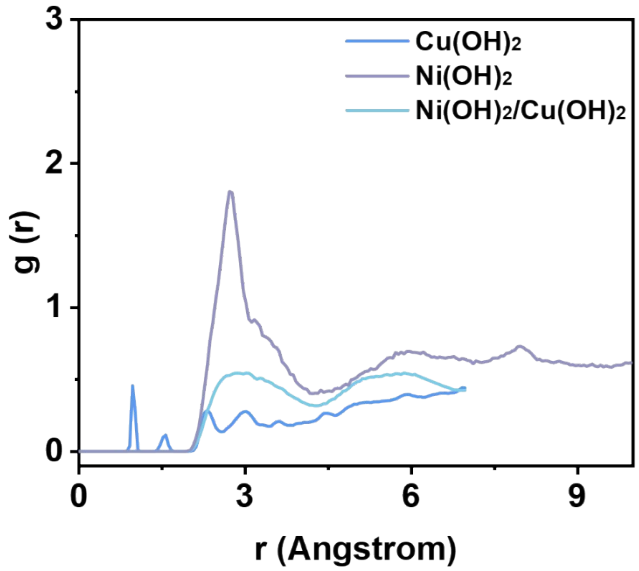

Fig. S19. RDF of H_2O molecules in the system of $Cu(OH)_2$, $Ni(OH)_2$ and $Ni(OH)_2/Cu(OH)_2$.

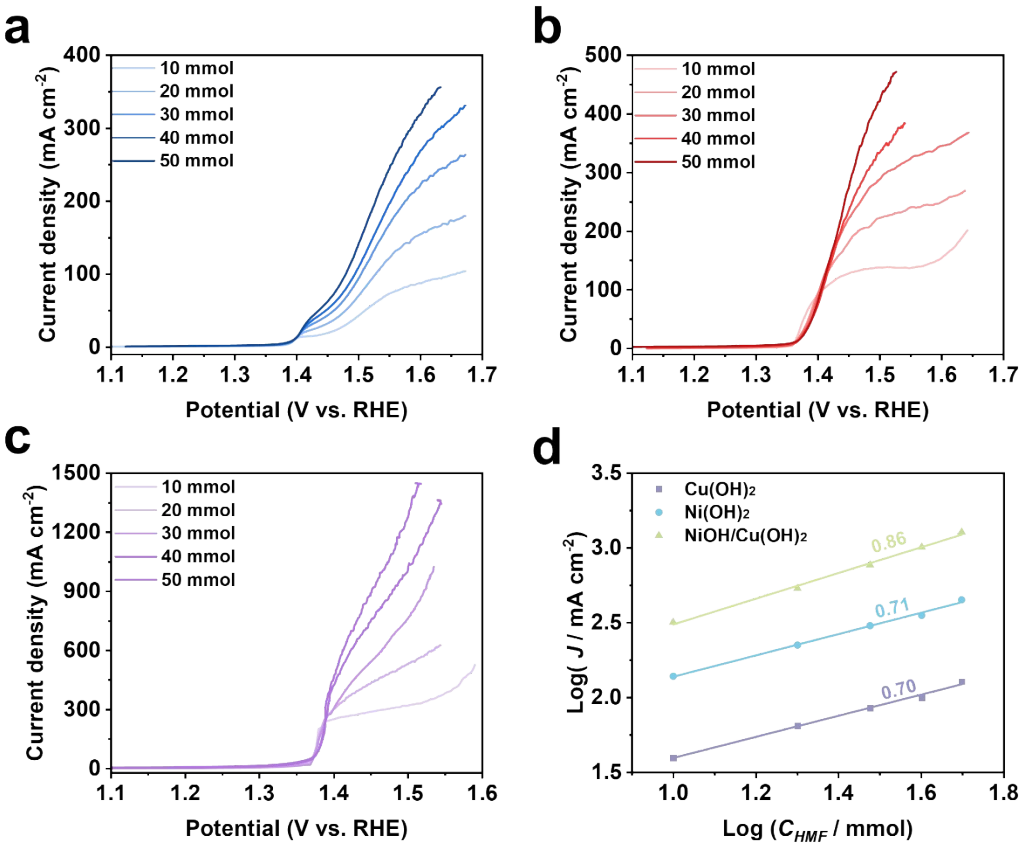

Fig. S20. LSV curves of (a) $Cu(OH)_2$, (b) $Ni(OH)_2$ and (c) $Ni(OH)_2/Cu(OH)_2$ in 1 M KOH with different concentration of HMF; (d) partial current density for HMFOR as a function of HMF concentration in 1 M KOH over $Cu(OH)_2$, $Ni(OH)_2$ and $Ni(OH)_2/Cu(OH)_2$.

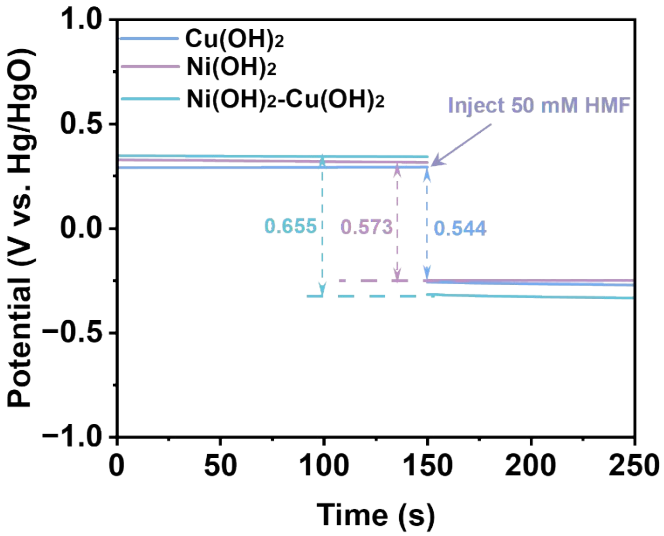

Fig. S21. OCP curves of $Cu(OH)_2$, $Ni(OH)_2$ and $Ni(OH)_2/Cu(OH)_2$ before and after injecting 50 mM HMF into electrolyte.

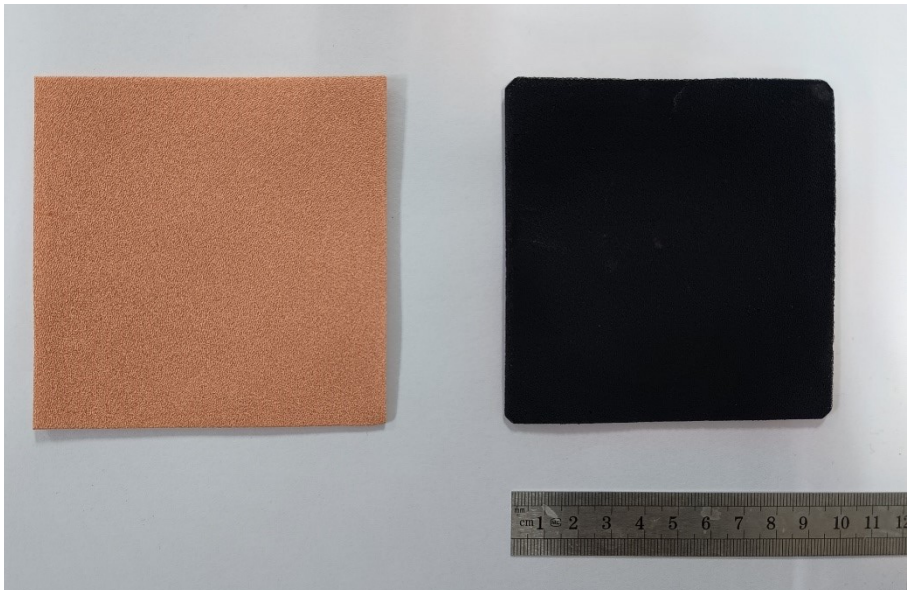

Fig. S22. The picture of Cu Foam (left) and obtained $Ni(OH)_2/Cu(OH)_2$/CF (right) in size 10 cm×10 cm.

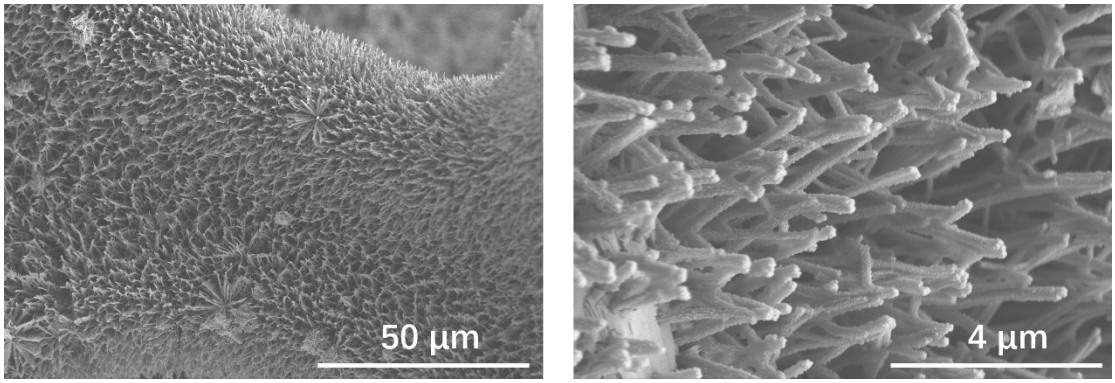

Fig. S23. SEM images of extended $Ni(OH)_2/Cu(OH)_2$ at different magnifications.

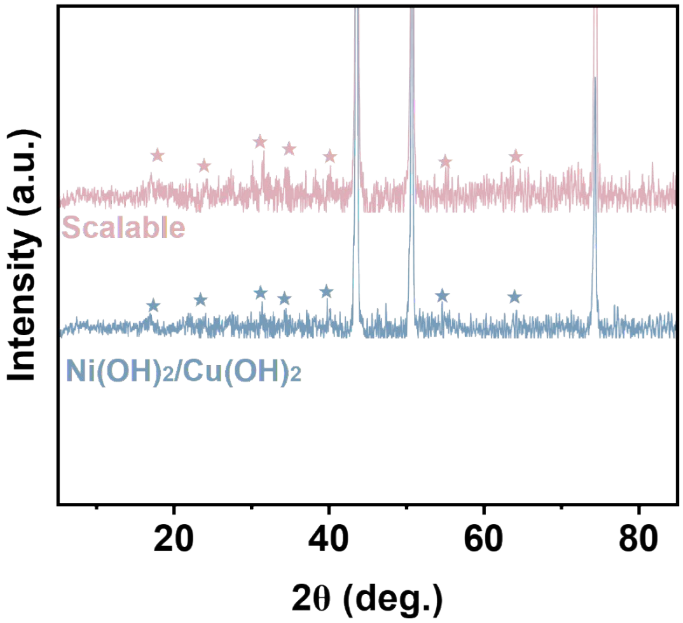

Fig. S24. XRD patterns of extended $Ni(OH)_2/Cu(OH)_2$.

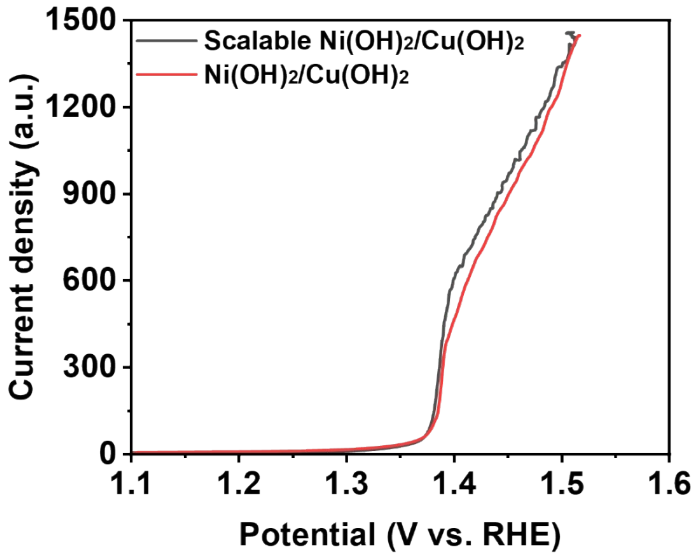

Fig. S25. LSV curves of extended and finely synthesized $Ni(OH)_2/Cu(OH)_2$.

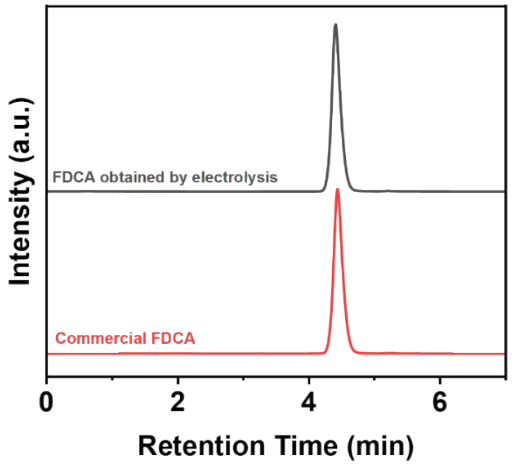

Fig. S26. High-performance liquid chromatography chromatograms of commercial FDCA and FDCA obtained by electrolysis.

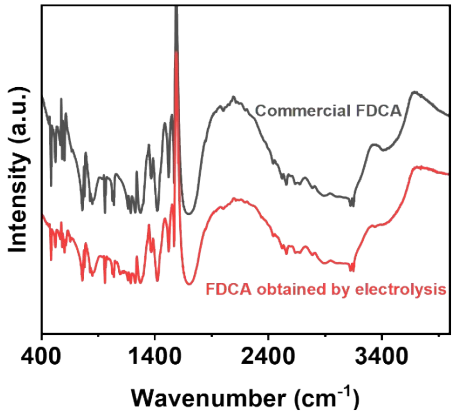

Fig. S27. FT IR spectra of commercial FDCA and FDCA obtained by electrolysis.

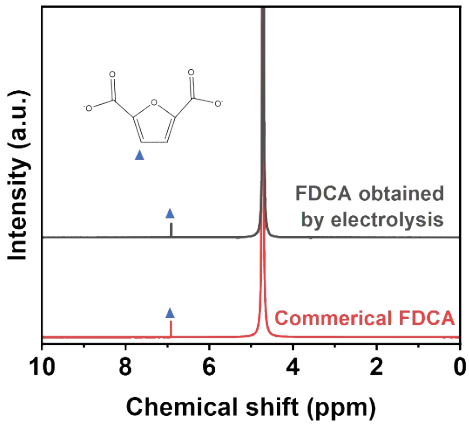

Fig. S28. ^{1}H NMR spectra of commercial FDCA and FDCA obtained by electrolysis.

Table S1. Comparison of HMF electrocatalytic performance of catalysts recently reported.

Catalyst	Maxinum current density ($mA\ cm^{-2}$)	Stability time (h)	Reference
$Ni(OH)_2/Cu(OH)_2$	1300	380	This work
NiB/CoOOH	250	110	1
Rh-NiFe	60	6.9	2
NiCo-LDH	150	16.7	3
PO_4/Ru-$Ni(OH)_2$	1000	2	4
NiCu/NF	1000	58	5
Cu/Ni_3S_2	200	12	6
Co@NiMoO-Ni	200	50	7
$NiCo_2$@MoO_2	220	6	8
Co-Ni_3S_2	600	3.3	9
Ni-Laser	40	90	10
Mn-NiS	600	1.67	11
Ni_3S_2/NiOx	500	100	12

References

1 H. G. Xu, X. R. Ning, J. Y. Zhao, H. Y. Lin, H. Q. Fu, S. Wang, Y. Guo, H. Wu, M. Zhu, H. Y. Yuan, P. F. Liu and H. G. Yang, Chem, 2024, 2147-2169.
2 L. Zeng, Y. Chen, M. Sun, Q. Huang, K. Sun, J. Ma, J. Li, H. Tan, M. Li, Y. Pan, Y. Liu, M. Luo, B. Huang and S. Guo, J. Am. Chem. Soc. 2023, 145, 17577-17587.
3 S.-Q. Liu, M.-R. Gao, S. Wu, R. Feng, Y. Wang, L. Cui, Y. Guo, X.-Z. Fu and J.-L. Luo, Energy Environ. Sci. 2023, 16, 5305-5314.
4 Z. Yang, S. Wang, C. Wei, L. Chen, Z. Xue and T. Mu, Energy Environ. Sci. 2024, 17, 1603-1611.
5 D. Chen, Y. Ding, X. Cao, L. Wang, H. Lee, G. Lin, W. Li, G. Ding and L. Sun, Angew. Chem. Int. Ed. 2023, 62, e202309478.
6 P. Xu, Z. Bao, Y. Zhao, L. Zheng, Z. Lv, X. Shi, H. E. Wang, X. Fang and H. Zheng, Adv. Energy Mater. 2023, 14, 2303557.
7 J. Wu, Z. Zhai, S. Yin and S. Wang, Adv. Funct. Mater. 2023, 34, 2308198.
8 J. Wu, J. Chen, T. Yu, Z. Zhai, Y. Zhu, X. Wu and S. Yin, ACS Catal. 2023, 13, 13257-13266.
9 Y. Sun, J. Wang, Y. Qi, W. Li and C. Wang, Adv. Sci. 2022, 9, 2200957.
10 J. Liu and S. Tao, Adv. Sci. 2023, 10, 2302641.
11 S. Li, S. Wang, Y. Wang, J. He, K. Li, Y. Xu, M. Wang, S. Zhao, X. Li, X. Zhong and J. Wang, Adv. Funct. Mater. 2023, 33, 2214488.
12 D. Xiao, X. Bao, D. Dai, Y. Gao, S. Si, Z. Wang, Y. Liu, P. Wang, Z. Zheng, H. Cheng, Y. Dai and B. Huang, Adv. Mater. 2023, **35**, 2304133.